Volume 14
Number 22
14 April 2026
Pages 13121–13888

Journal of Materials Chemistry A

Materials for energy and sustainability

rsc.li/materials-a

ISSN 2050-7488

ROYAL SOCIETY OF CHEMISTRY

PAPER

Joohyung Lee *et al.*

Light-on and power-on: a dual mode active de-/anti-icing system using liquid metal-based photothermal and electrothermal pastes

Journal of Materials Chemistry A

ROYAL SOCIETY OF CHEMISTRY

PAPER

View Article Online
View Journal | View Issue

Cite this: J. Mater. Chem. A, 2026, 14, 13363

Light-on and power-on: a dual mode active de-/anti-icing system using liquid metal-based photothermal and electrothermal pastes

Chimin Song,[a] Soonchul Kwon,[b] Jungmin Lee,[c] Yongmin Cho[a] and Joohyung Lee *[a]

Ice accumulation on surfaces in cold environments poses persistent safety and operational challenges across diverse sectors, including transportation, aviation, outdoor equipment, residential buildings, and industrial facilities. In this study, we present a dual-mode de-/anti-icing platform that synergistically integrates the photothermal and electrothermal functionalities of Ga-based liquid metals (LMs). The photothermal component, consisting of micronized LM droplets hybridized with a phase change material (PCM), efficiently converts solar irradiation into heat while self-regulating surface temperature through latent heat absorption under varying seasonal conditions. Separately, the electrothermal component maintains LM continuity and is engineered with Si fillers to enable printable Joule heating with tunable electrical and thermal properties. Both components are formulated as viscoelastic pastes with excellent rheological processability, allowing direct and customizable application to diverse substrates. When sequentially integrated, the system demonstrates reliable and energy-efficient performance, achieving rapid surface heating and effective prevention of ice formation under simulated winter conditions, including overcast and nighttime scenarios. Owing to its ease of application and high performance, the system offers a practical and effective solution for ice management across diverse operational and environmental contexts.

Received 20th December 2025
Accepted 2nd February 2026

DOI: 10.1039/d5ta10376b

rsc.li/materials-a

Introduction

Ice formation in cold climates poses a significant threat to the safe operation of transportation systems, aircraft, outdoor infrastructure, residential buildings, and industrial facilities.[1–3] With extreme and unpredictable weather events becoming increasingly frequent due to climate change, the demand for effective de-icing and anti-icing technologies continues to grow.[4–6] In response, extensive research efforts[4–18] have been devoted to developing alternative strategies that can supplant conventional chemical and mechanical methods, which are often labor-intensive, resource-consuming, and costly. Among these, active de-/anti-icing techniques based on photothermal and electrothermal effects have recently garnered considerable attention. Photothermal de-/anti-icing relies on specific classes of materials that efficiently convert incident solar irradiation into heat,[19] thereby increasing the temperature of the host surface above the ice melting point during daylight hours and preventing ice accumulation.[7–10] This strategy offers the advantage of harnessing sustainable solar energy without the need for external power input. However, its performance is inherently limited under overcast conditions or at night, when solar irradiance is insufficient or entirely absent.[7] In contrast, electrothermal de-/anti-icing systems rely on Joule heating generated by electrically conductive materials at an applied voltage, offering consistent and controllable thermal energy regardless of weather conditions or time of day.[11,12] Traditional systems typically employ embedded solid-state heating cables, which require labor-intensive underground installation and may be restricted by terrain, safety regulations, or environmental constraints. Recently, surface-applied conductive coatings composed of carbon- or ceramic-based materials have emerged as promising alternatives.[11–18] Achieving high de-/anti-icing performance in such systems requires careful optimization of the surface's electrical properties, often through fine-tuning the concentration of conductive agents; however, this can potentially compromise the coating's processability or mechanical robustness. Dual-mode systems that combine photothermal and electrothermal mechanisms offer strong potential for maximizing de-/anti-icing efficiency with minimal energy consumption under diverse weather conditions and timeframes.[13–18] Nonetheless, enabling the seamless integration of both functionalities and achieving independent control over

[a]Department of Chemical Engineering, Myongji University, 116 Myongji-ro, Cheoin-gu, Yongin, Gyeonggi-do, 17058, Korea. E-mail: ljbro@mju.ac.kr
[b]Department of Civil and Environmental Engineering, Pusan National University, 2 Busandaehak-ro 63beon-gil, Geumjeong-gu, Busan, 46241, Korea
[c]Land & Housing Institute, Korea Land & Housing Corporation, 462-2 Jeonmin-dong, Useong-gu, Daejeon, 305-731, Korea

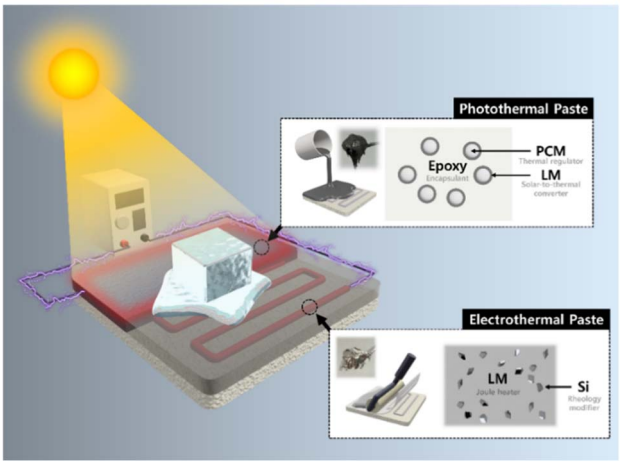

Fig. 1 Schematic illustration of the dual-mode de-/anti-icing system, fabricated by integrating the photothermal and electrothermal pastes based on Ga-based LMs.

each mechanism across arbitrary application sites and environmental conditions may involve nontrivial design considerations.

Low-melting-point metals such as Ga and eutectic Ga–In (EGaIn), which often melt near or below room temperature and are commonly referred to as liquid metals (LMs), combine the intrinsic properties of metals—such as high electrical and thermal conductivity and plasmonic behavior—with the fluidic and deformable characteristics of liquids.[20] These unique features have attracted significant attention across a wide range of advanced applications.[21] In this study, we considered the LM as a multifunctional source material for photothermal and electrothermal de-/anti-icing, leveraging its unique combination of efficient photothermal conversion and high electrical conductivity as well as its excellent rheological processability. As a first step, a photothermal paste was developed by dispersing LM as a filler in a curable polymer matrix (Fig. 1). When dispersed as micronized droplets, LM efficiently converts broadband solar irradiation into heat, enabling solar-mediated de-/anti-icing under cold-weather conditions without external energy input. While high solar-to-thermal conversion efficiency is undoubtedly beneficial for de-/anti-icing in winter, it becomes less desirable in summer, as it can cause unnecessary overheating of the surrounding environment. To address this limitation, we developed a self-thermoregulating hybrid photothermal converter by incorporating LM with a phase-change material (PCM).[22] The PCM was chosen with a melting point close to typical summer ambient temperatures, enabling suppression of excessive temperature increases through latent heat absorption during its solid–liquid transition at elevated temperatures. The resulting composite filler provides passive thermal regulation of the photothermal paste in hot environments, while maintaining efficient solar-to-thermal conversion under cold conditions, thereby achieving seasonally adaptive performance. Separately, to ensure de-/anti-icing functionality even in the absence of sunlight—such as during overcast weather or nighttime—an LM-based electrothermal paste was developed (Fig. 1). Unlike the photothermal paste, in which LM droplets are dispersed in a polymer matrix, this electrothermal paste utilizes LM as a continuous, conductive matrix. By incorporating an optimized amount of fillers into the fluidic bulk LM, printable rheological properties were achieved. This enabled direct patterning of the resulting paste onto target substrates, providing a versatile platform for the fabrication of highly customized electrothermal de-/anti-icing systems with tunable electrical conductivity and thermal output, representing a significant departure from conventional strategies. The developed photothermal/electrothermal paste kit based on soft LM—each component exhibiting highly processable rheological properties—can be sequentially applied onto arbitrary substrates to construct a combined dual-mode de-/anti-icing system. This integrated platform operates under simulated winter conditions with various illumination levels, powered by light and/or electricity, and thus represents a promising platform for active surface de-/anti-icing.

Results and discussion

The hybrid filler composed of a LM and PCM for photothermal paste can be easily and scalably prepared by simply adding micronized PCM into bulk LM and mixing them. We employed Ga—the most extensively studied LM[20,21]—as the photothermal component. As the thermal regulator PCM, we selected *n*-eicosane, which has a melting point ($\approx$37 °C) similar to the average maximum summer temperatures in Seoul, South Korea, as a proof of concept. (Depending on the target region, PCMs with different melting points could be appropriately chosen to match local summer temperatures. For details on the phase-change behavior of LM–PCM mixtures depending on the type of PCM used, please refer to our earlier study[23,24]). Bulk *n*-eicosane was first emulsified in an aqueous surfactant solution and then freeze-dried to produce fine particulate powders, which were subsequently introduced into liquid-phase bulk Ga (Fig. 2(a1)) and homogenized *via* planetary mixing. At low PCM loadings, the mixture exhibited a highly viscous, paste-like morphology (Fig. 2(a2)), closely resembling the previously reported colloidal PCM-in-LM emulsion structure, in which PCM microparticles were suspended within a continuous LM matrix.[23] In contrast, when the PCM content exceeded approximately 60 vol%, the mixture transformed into a powder-like material (Fig. 2(a3)) similar in morphology to the original PCM, albeit with a grayish hue. Optical microscopy images of the mixture with a PCM-to-Ga volume ratio of 63.4 : 36.6 (Fig. 2(c1)) revealed dark-colored particles, distinct from the translucent appearance of the pure PCM (Fig. 2(b1)), indicating surface coating by light-blocking metallic Ga. After Ga coating, the average particle size increased by approximately 12%, from 8.31 $\pm$ 0.37 μm for pure PCM microparticles to 9.43 $\pm$ 0.21 μm (see Fig. S1(a) and (b) for detailed size distributions), suggesting that the Ga coating layer on the PCM surface was formed as a thin shell with a thickness on the order of $\sim$1 μm. Further scanning electron microscopy (SEM) analysis revealed that, unlike the relatively soft and waxy surface texture of the pure PCM particles (Fig. 2(b2)), the hybrid particles exhibited a rougher morphology with their surfaces

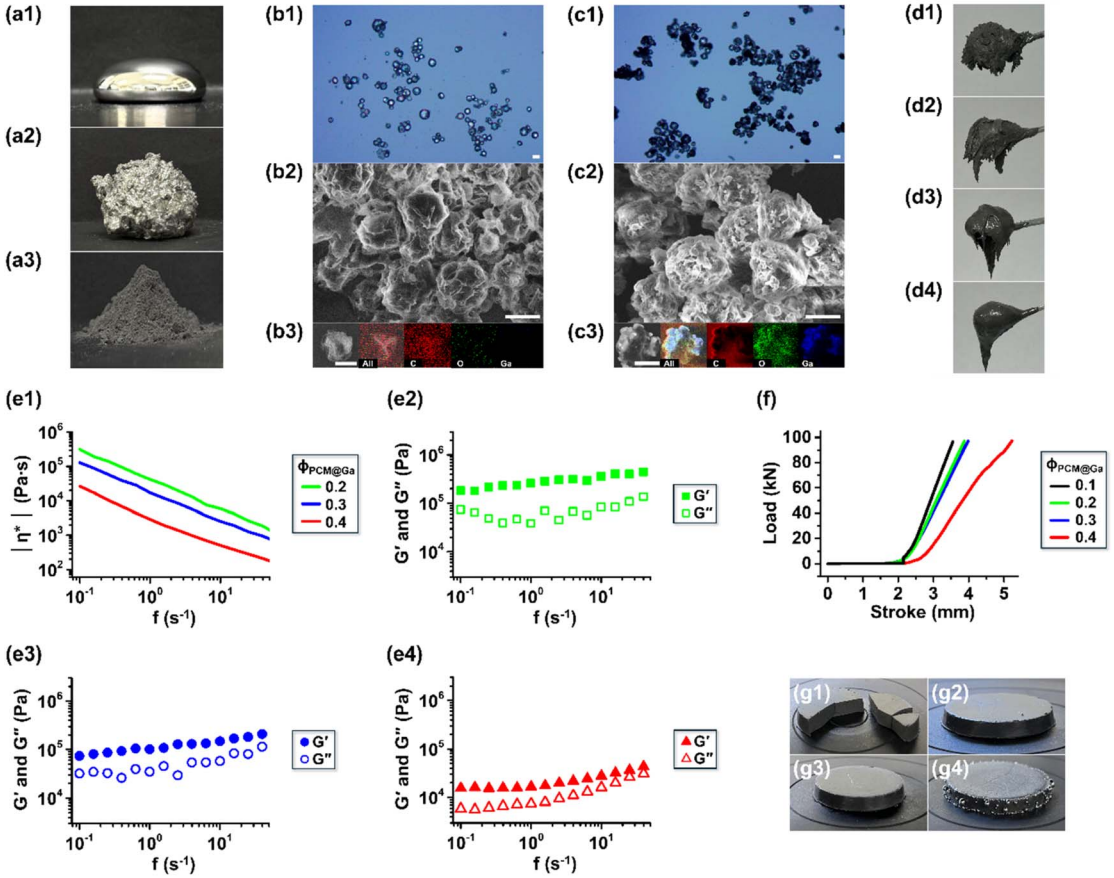

Fig. 2 (a) Photographs of (a1) pure Ga and mixtures of Ga and micronized PCM with PCM-to-Ga volume ratios of (a2) 58.4 : 41.6 and (a3) 63.4 : 36.6. (b and c) Morphological analysis of (b) micronized PCM and (c) PCM@Ga: (b1 and c1) optical micrographs, (b2 and c2) SEM images, and (b3 and c3) elemental mapping images *via* EDS (scale bars: 10 μm). (d) Visual appearances of photothermal pastes with various $\phi_{PCM@Ga}$: (d1) 0.1, (d2) 0.2, (d3) 0.3, and (d4) 0.4. (e) Rheological measurements of the photothermal pastes: (e1) complex viscosities for different $\phi_{PCM@Ga}$, and elastic and viscous moduli for (e2) $\phi_{PCM@Ga} = 0.2$, (e3) 0.3, and (e4) 0.4. For all rheological measurements, ϕ_F was fixed at 0.5. No catalysts were added to the formulations in order to allow fair comparison of their relative fluidities while suppressing spontaneous curing during the measurements. (f) Load-stroke curves of the cured photothermal paste specimens under 100 kN compression loading. (g) Post-compression visual appearances of the specimens with different $\phi_{PCM@Ga}$: (g1) 0.1, (g2) 0.2, (g3) 0.3, and (g4) 0.4.

densely populated by numerous fine particulates (Fig. 2(c2)), which are presumably Ga microdroplets approximately one order of magnitude smaller in size. Elemental mapping by energy dispersive spectroscopy (EDS) on a partially melted, isolated hybrid particle (Fig. 2(c3)) confirmed the presence of a carbon-rich PCM core encapsulated by Ga (additional analysis of a fully encapsulated hybrid particle is provided in Fig. S1(c)), whereas no Ga signal was detected in the pristine PCM particles (Fig. 2(b3)). This hybrid structure, hereafter referred to as PCM@Ga, features a particle size of approximately 10 μm and can be readily obtained through direct mixing, without the need for pre-micronization of Ga—a process that is typically time-consuming and technically demanding.[25] The resulting powder, serving as a functional filler, can be conveniently quantified and dispersed into a polymer matrix along with other components for composite fabrication.

To produce photothermal pastes, varying amounts of PCM@Ga were incorporated into a curable alumina-reinforced epoxy (ARE) solution. Fig. 2(d) and (e) show the visual appearances and the measured rheological properties of the resulting photothermal pastes, which are colloidal suspensions of PCM@Ga. Overall, at a fixed total filler volume fraction ($\phi_F = \phi_A + \phi_{PCM@Ga} = 0.5$, where ϕ_A and $\phi_{PCM@Ga}$ denote the volume fractions of alumina and PCM@Ga, respectively), a noticeable decrease in the stiffness of the paste was observed as the fraction of PCM@Ga—with its compliant liquid Ga surface coating—increased. For example, the magnitude of the complex viscosity ($|\eta^*|$) decreased by approximately an order of magnitude as $\phi_{PCM@Ga}$ increased from 0.2 to 0.4 (Fig. 2(e1)). (Note: measurements for the formulation with $\phi_{PCM@Ga} = 0.1$ could not be performed due to its exceedingly high viscosity; this paste exhibited severe adhesion to the mixing unit after processing, making even sample retrieval extremely difficult-see Fig. S2). This enhanced flowability would facilitate easier application of the paste onto designated areas. Meanwhile, the component analysis of the measured complex viscosity (Fig. 2(e2)–(e4)) reveals that, across the entire frequency range tested, the elastic modulus (G') consistently exceeded the viscous modulus (G''). This indicates that, despite the structural softening induced by higher PCM@Ga loadings, the paste

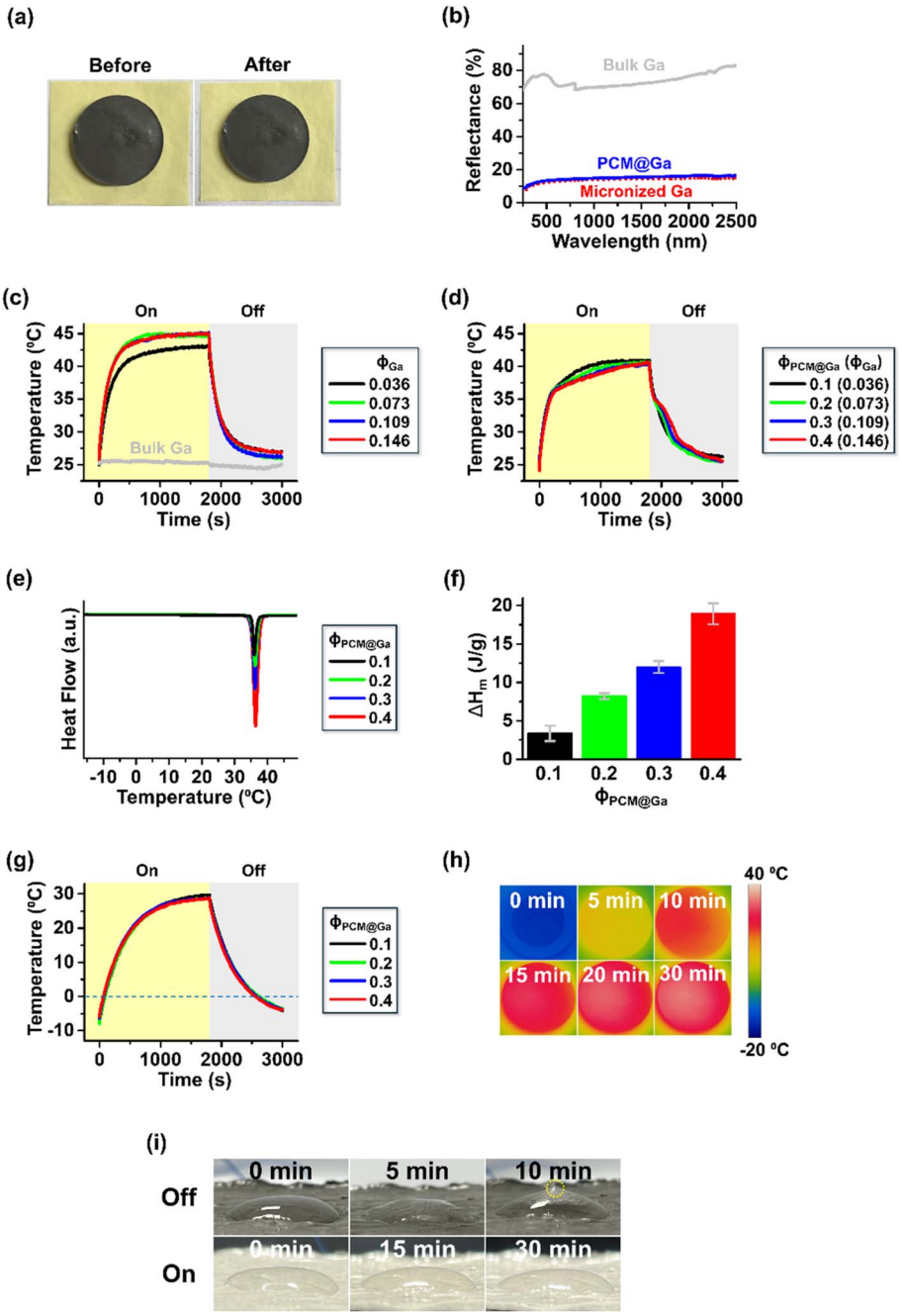

Fig. 3 (a) Photographs of the cured photothermal pastes ($\phi_{PCM@Ga} = 0.3$) placed on oil-absorbing paper, taken before (left) and after (right) heating at 50 °C for 30 min. (b) Surface reflectance spectra of bulk Ga and cured photothermal composites containing either micronized Ga or PCM@Ga (both with $\phi_{Ga} = 0.109$). (c and d) Surface temperature profiles of the cured composites containing (c) Ga and (d) PCM@Ga with various loadings under 1 sun irradiation at ambient temperature. (e) DSC profiles of the cured composites during a temperature ramp and (f) the corresponding ΔH_m values (n: 3). (g) Surface temperature profiles of the composites containing PCM@Ga under simulated solar irradiation (1 sun) in a cold environment (−20 °C). Here, −20 °C denotes the ambient air temperature inside the environmental chamber, while the initial surface temperature corresponds to the quasi-steady thermal state of the composite, determined by air–surface heat transfer and the thermal inertia of the bulk material. (h) Representative IR images of the photothermally heated specimen ($\phi_{PCM@Ga} = 0.3$) at −20 °C, taken at various time intervals. (i) Observations of 400 μL water droplets on the surface of the cured composites at −20 °C, without (top) and with (bottom) 1 sun irradiation.

maintains a robust, solid-like rheological character, even at the highest PCM@Ga loading. Such formability ensures reliable installation and shaping of the photothermal paste directly onto target surfaces without risk of leakage.

Using photothermal pastes containing various PCM@Ga loadings, disk-shaped composite specimens with flat surfaces were fabricated *via* thermal curing (Fig. 3(a)), and their temperature evolution over time was measured under

simulated solar irradiation (1 sun, 0.1 W cm^{-2}) at room temperature (25 °C). It is worth noting that bulk Ga primarily exhibits plasmon resonance behavior in the ultraviolet (UV) region and has therefore not been commonly considered a broadband solar-to-thermal conversion material.[26] As a control, we confirmed that bulk Ga strongly reflected incident light across the solar spectrum range of 250–2500 nm (Fig. 3(b)) and exhibited only a minimal surface temperature increase under simulated solar irradiation (Fig. 3(c)). However, when Ga is dispersed into small droplets and surrounded by a dielectric medium, it can exhibit localized surface plasmonic responses extending well beyond the UV region through metal–dielectric coupling and enhanced light absorption/scattering effects,[19,27] which have been widely exploited in other fields, including biomolecular engineering.[28–30] In line with these findings, we fabricated bulk Ga into microdroplets *via* sonication and dispersed them in a non-metallic, dielectric ARE matrix (Fig. S3). The resulting composite exhibited markedly lower reflectivity across the broadband solar spectrum (Fig. 3(b)) and demonstrated significantly enhanced photothermal conversion performance (Fig. 3(c)). Upon 30 min of simulated solar irradiation, the pristine ARE matrix without Ga exhibited a modest temperature increase (ΔT) of only 8.6 °C (Fig. S4). In contrast, specimens containing Ga microdroplets reached $\Delta T = 19.6$ °C at the highest Ga content, demonstrating the excellent photothermal conversion capability of Ga. The observed ΔT and the corresponding photothermal conversion efficiency of 78.09% (SI) fall within the range reported for high-performance photothermal LM composites precisely coupled with light-absorbing matrices.[31–33] This efficiency is comparable to, or even surpasses, those reported for other metal-, semiconductor-, and polymer-based photothermal converters.[19]

As noted earlier, such high photothermal conversion efficiency is undoubtedly advantageous for winter de-/anti-icing applications; however, it could lead to undesirable heating of the surrounding environment in summer. As shown in Fig. 3(d), unlike the Ga-only specimens, all composites loaded with the hybrid filler, PCM@Ga, exhibited pronounced retardation in the temperature increase near the melting temperature of the PCM (≈37 °C). Note that the inclusion of PCM has a negligible effect on the overall thermal conductivity of the composite, as the thermal conductivity of the PCM (≈0.1–0.2 W m^{-1} K^{-1}) is comparable to that of the epoxy matrix.[23,34] For instance, the composite with $\phi_{PCM@Ga} = 0.3$ (comprising PCM and Ga fractions of 0.191 and 0.109, respectively) exhibited a thermal conductivity of 0.785 ± 0.004 W m^{-1} K^{-1}, which is close to that of the corresponding PCM-free control composite (0.721 ± 0.015 W m^{-1} K^{-1}) containing the same Ga fraction (0.109) and an equivalent extra epoxy fraction (0.191) (SI). Therefore, the observed retardation in the temperature increase near the PCM melting point can be attributable to latent heat absorption during the solid–liquid phase transition of the encapsulated PCM, rather than to any change in the overall thermal conductivity of the composite. Interestingly, despite the increased photothermal Ga content at higher hybrid filler loadings, the temperature increase was further suppressed. This can be attributed to enhanced latent heat absorption due to the simultaneously increased PCM content, as evidenced by the progressively growing endothermic peak in the differential scanning calorimetry (DSC) profiles (Fig. 3(e)) and the increase in melting enthalpy (ΔH_m; Fig. 3(f)) with increasing $\phi_{PCM@Ga}$. At the highest filler loading, the measured ΔH_m was 18.9 ± 1.3 J g^{-1}, which is close to the theoretically calculated value of 19.1 J g^{-1} based on the composition ratio. This result indicates that the latent heat absorption associated with the intrinsic phase transition of the paraffinic PCM is not significantly affected by any potential chemical reaction with the LM, consistent with previous studies.[23,24] As a result, in the specimen with the highest hybrid filler loading ($\phi_{PCM@Ga} = 0.4$, where $\phi_{Ga} = 0.146$), the final surface temperature after 30 min of simulated solar irradiation was ≈40 °C, whereas that of the PCM-free specimen with the same Ga content ($\phi_{Ga} = 0.146$) reached ≈45 °C, demonstrating that the hybrid filler can provide a temperature suppression effect of approximately 5 °C under elevated thermal conditions. Notably, no leakage of the PCM was observed during temperature suppression *via* its solid–liquid transition (Fig. 3(a)), indicating robust encapsulation of the PCM within the composite. In addition, we confirmed that nearly identical DSC results were obtained for the composite samples stored for more than six months (Fig. S5), further demonstrating the long-term reliability and thermal stability of the fabricated system.

The PCM@Ga-loaded composites were subsequently exposed to cold conditions (−20 °C) and irradiated with a solar simulator to evaluate whether these materials function as effective solar-to-thermal converters suitable for de-/anti-icing applications—the primary objective of this study. As shown in Fig. 3(g) and (h), the surface temperature increased rapidly, reaching the melting point of ice (0 °C) from an initial temperature of −10 °C within approximately 1 min. Continued irradiation resulted in a final surface temperature of ≈30 °C after 30 min for all tested samples. This corresponds to a temperature increase (ΔT) of ≈40 °C, which notably exceeds the ΔT of ≈15 °C observed under ambient conditions over the same irradiation period. Owing to this elevated surface temperature, a water droplet placed on the composite surface did not freeze for an extended period under simulated solar irradiation (Fig. 3(i)). Importantly, because the final surface temperature under these cold conditions remained below the melting point of the PCM (≈37 °C), the temperature-retardation effect associated with latent heat absorption—previously observed under ambient conditions—was not present (Fig. 3(g)). These results highlight a key advantage of the PCM@Ga-based hybrid photothermal fillers: increasing their loading enables equivalently rapid surface heating under cold winter conditions to achieve effective de-/anti-icing, while simultaneously suppressing the excessive temperature increase in hot summer environments through autonomous thermal buffering.

Incorporating a sufficient amount of PCM@Ga in the photothermal composite formulation can be beneficial not only for achieving seasonally optimized solar-to-thermal conversion, but also for enhancing the processability of the paste prior to curing. However, excessive loading may compromise the

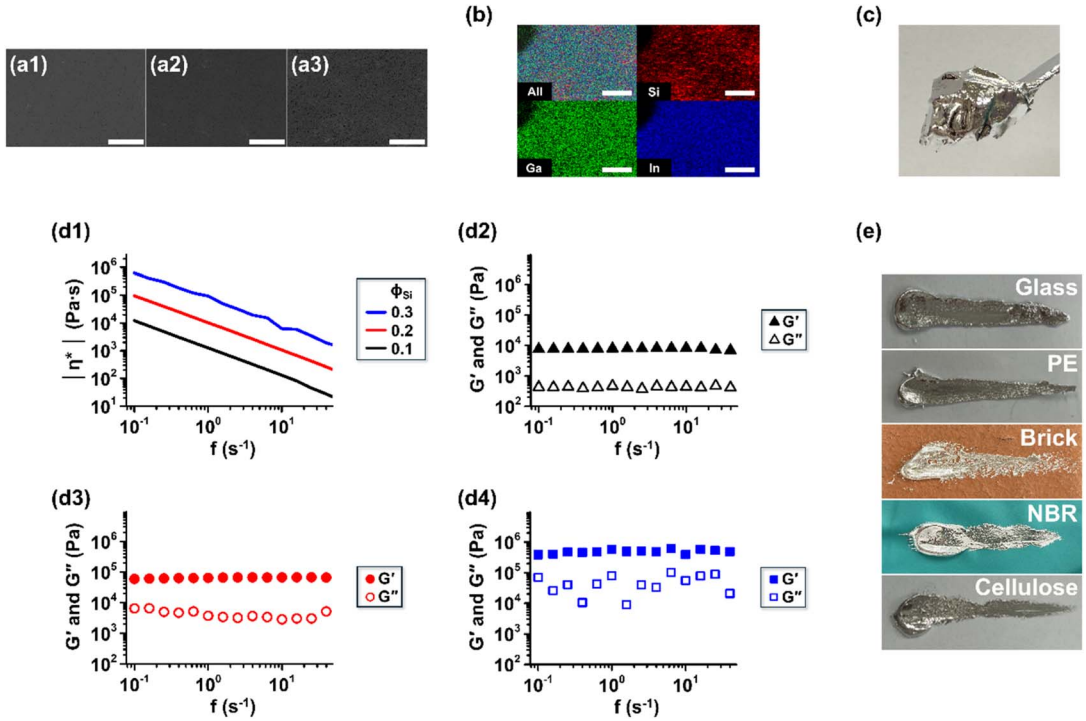

Fig. 4 (a) SEM images of the electrothermal pastes with different ϕ_{Si}: (a1) 0.1, (a2) 0.2, and (a3) 0.3. (b) EDS elemental mapping of the paste with $\phi_{Si} = 0.3$ (scale bars: 10 μm). (c) Photograph of the paste with $\phi_{Si} = 0.3$. (d) Rheological properties of the electrothermal pastes: (d1) complex viscosities for different ϕ_{Si}, and elastic and viscous moduli for (d2) $\phi_{Si} = 0.1$, (d3) 0.2, and (d4) 0.3. (e) Photographs of the pastes ($\phi_{Si} = 0.3$) spread on various substrates (PE: polyethylene; NBR: nitrile butadiene rubber).

mechanical integrity of the cured composite. Fig. 2(f) and (g) presents the deformation behavior of cured composite specimens with different PCM@Ga volume fractions ($\phi_{PCM@Ga} = 0.1$, 0.2, 0.3, and 0.4), prepared under a fixed total filler volume fraction ($\phi_F = 0.5$), subjected to a compressive load of up to 100 kN—equivalent to the weight of a 10-ton truck—applied perpendicularly to the surface. In the specimen with the highest PCM@Ga content ($\phi_{PCM@Ga} = 0.4$), a substantial reduction in thickness was observed under load due to excessive deformation, accompanied by severe leakage of liquid Ga from the interior. In contrast, in specimens containing either no PCM@Ga (Fig. S6) or only a small amount ($\phi_{PCM@Ga} = 0.1$), the composites were overly rigid, exhibiting minimal deformation but fracturing at relatively low loads. Notably, samples with intermediate PCM@Ga loadings ($\phi_{PCM@Ga} = 0.2$ and 0.3) exhibited moderate and stable deformation up to the maximum load of 100 kN, without mechanical failure or Ga leakage, thereby demonstrating the most desirable mechanical performance. The formulation with $\phi_{PCM@Ga} = 0.3$ was therefore selected for subsequent integration with the electrothermal system, as it provides an optimal balance among thermal performance, processability prior to curing, and mechanical robustness after curing.

The as-prepared photothermal system can serve as a coating layer on other active de-/anti-icing systems, ensuring functionality even under non-solar conditions, such as overcast or nighttime environments. One example is the acoustic approach,[35] which employs mechanical vibrations to detach ice with minimal energy loss and offers excellent potential for rapid de-icing within a desired timeframe. However, such systems generally involve complex fabrication procedures and may face challenges when applied to arbitrary substrates with irregular surface properties or geometries; moreover, further research is required to achieve scalable, large-area implementation. Another representative method is the Joule-heating-based electrothermal system. Although this approach may induce relatively higher power consumption, such energy demand can be mitigated through synergistic operation with the overlying photothermal system, while offering greater design flexibility. Unlike conventional rigid wiring or recently developed film-type electrothermal systems,[11–18] our formulation strategy utilizes a LM to realize a scalable, printable electrothermal paste that can be directly patterned onto arbitrary substrates in a customizable and adaptable manner.

To develop a printable liquid-state electrothermal system compatible with the photothermal system described above, a eutectic alloy of Ga and In (EGaIn) was employed. Adding In to Ga lowers the melting point to 16 °C, significantly below that of pure Ga (30 °C), enabling the alloy to remain a stable, low-viscosity liquid (≈2 Pa s) at ambient temperature.[20] Unfortunately, in its bulk form, this LM exhibits high surface tension and poor wettability on most substrates.[23] Combined with its low viscosity, these properties limit its ability to form high-resolution patterns suitable for Joule heating. To improve printability, fillers were introduced into the bulk LM. Unlike the photothermal paste described earlier, where LM was dispersed

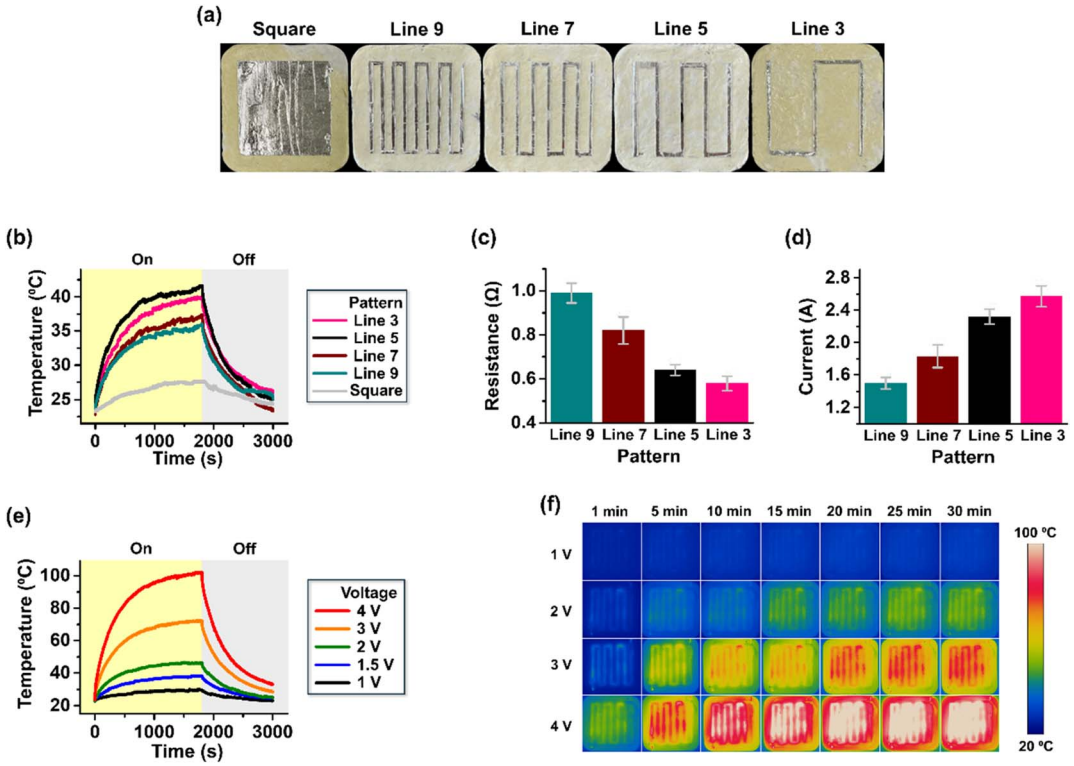

Fig. 5 (a) Screen-printed electrothermal patterns ($\phi_{Si} = 0.3$) spanning a 5 cm × 5 cm area on the surface of cured ARE matrices. (b) Average temperature profiles within the 4 cm × 4 cm area containing various electrothermal patterns at an applied voltage of 1.5 V at ambient temperature. (c) Electrical resistances of the different patterns (n: 5). (d) Measured currents at an applied voltage of 1.5 V (n: 5). (e) Average temperature profiles within the 4 cm × 4 cm area containing the Line 7 pattern at various applied voltages. (f) IR images of the patterned area at various applied voltages, taken at different time intervals. In all temperature plots, the yellow and gray regions indicate the power-on (30 min) and power-off (20 min) periods, respectively.

as microdroplets within an ARE matrix, the electrothermal paste requires the LM to remain a continuous phase to allow current flow.[23] For this purpose, cost-effective and thermally conductive Si powder was used as a filler. Among various high-thermal-conductivity materials, Si exhibits favorable wettability with Ga-based LMs *via* interfacial oxides,[36–41] enabling uniform dispersion without disrupting metallic continuity or fragmenting the LM into discrete particles. A clear increase in the number concentration of filler particles dispersed within the matrix, associated with the increase in filler loading (from $\phi_F = \phi_{Si} = 0.1$ to 0.3), was observed *via* SEM (Fig. 4(a1)–(a3)). The uniform distribution of the Si element without noticeable segregation was further confirmed by EDS mapping (Fig. 4(b)). Fig. 4(c) shows the macroscopic appearance of the electrothermal paste with $\phi_{Si} = 0.3$, in which metallic EGaIn remains as a continuous phase, exhibiting a characteristic metallic luster. The measured thermal conductivity of this paste was 26.793 ± 1.071 W m^{-1} K^{-1}, which is very close to that of pure EGaIn (26.4 W m^{-1} K^{-1}).[23] This result indicates that heat transfer is predominantly governed by electron conduction through the preserved continuous LM phase, while the suspended Si particles do not degrade the overall thermal conductivity—unlike certain poorly conductive or less LM-compatible fillers reported previously.[23] Moreover, as the Si content dispersed in the matrix increased from $\phi_{Si} = 0.1$ to 0.3, the electrical resistance decreased by only 6.57% (Fig. S7), further confirming the preservation of the continuous LM phase.

As shown in Fig. 4(d1), the $|\eta^*|$ of the paste increased significantly with higher filler content. Notably, despite the LM remaining in a flowable continuous phase, the viscosity of the $\phi_{Si} = 0.3$ sample exceeded that of the ARE-based photothermal paste—designed for application on the outermost surface—by 1–2 orders of magnitude. Furthermore, for all formulations, the G' dominated the G'', and both G' and G'' increased consistently with increasing filler content (Fig. 4(d2)–(d4)), indicating enhanced shape retention of the pastes—a desirable property for patterning. These pastes could be readily applied onto various substrates regardless of their surface characteristics, whether hydrophilic or hydrophobic, and smooth or rough (Fig. 4(e)). This favorable applicability likely stems not only from the improved structural integrity but also from the formation of multiple adhesion points by the suspended Si particles.[36]

Fig. 5(a) shows the result of screen-printing various Joule heating patterns, each covering a square area of 5 cm × 5 cm, using the fabricated electrothermal paste and a stencil mask onto the surface of the cured ARE matrix. When the entire square area was coated with the paste and a voltage of 1.5 V was applied, the generated heat dissipated rapidly due to the large surface area, resulting in a significantly lower temperature

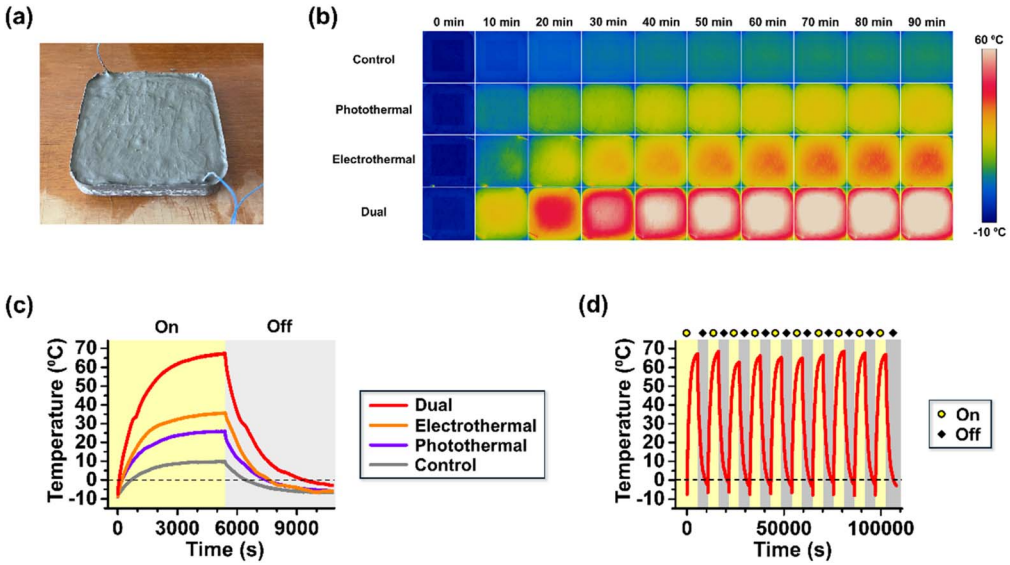

Fig. 6 (a) Photograph of the integrated photo/electrothermal de-/anti-icing system. (b) IR images of the system surface in different operation modes: photothermal (1 sun), electrothermal (2 V), and dual modes. (c) Average temperature profiles measured within the 4 cm × 4 cm central area of the surface. (d) Repeatability of dual-mode heating performance of the integrated system.

increase compared to that observed for line-shaped patterns at the same applied voltage (Fig. 5(b)). As the pattern length decreased, the electrical resistance was reduced (Fig. 5(c)), leading to higher current flow at the same applied voltage (Fig. 5(d)). Interestingly, this resulted in an increased peak temperature as the pattern shifted from a Line 9 to a Line 5 configuration, despite the decreasing coverage of the electrothermal system on the substrate (Fig. 5(b)). In the case of Line 3, although the current flow was even greater than that of Line 5, the uncovered substrate area became excessively large, causing a slight reduction in the peak temperature. These results underscore the importance of designing a thermally optimized electrothermal pattern tailored to the target surface area for efficient heating. This can be readily accomplished using the excellent printability of the LM-based paste developed in this study. Unlike conventional de-/anti-icing electrothermal systems—where tuning electrical properties typically requires changes in material composition, often at the expense of mechanical strength, processability, or other critical parameters—our printable electrothermal system offers a distinct advantage: it enables versatile control over electrical properties simply by modifying the printed pattern, without altering the optimized formulation. More fundamentally, we remark that the present paste-mediated, single-step, room-temperature printing approach enables fabrication of electrothermal systems without the complex, multi-step, equipment-intensive processes often used in prior de-/anti-icing systems, such as vacuum-based thin-film deposition, high temperature consolidation/sintering, or multi-step lamination of heating elements. This process simplicity provides a viable route to drastically reduce the manufacturing cost essential for scalable fabrication, even though Ga-based LM itself is not a low-cost material.

Fig. 5(e) and (f) present the average temperature evolutions within the 4 cm × 4 cm surface area containing the selected pattern (Line 7) at varying applied voltages during Joule heating. As the applied voltage increased, the peak temperature achieved within the same time frame increased systematically. At the maximum applied voltage of 4 V, a rapid temperature increase of ΔT = 19.1 °C was observed within 1 min, and the peak temperature reached as high as ΔT = 78.7 °C after 30 min. This tunability of surface heating with respect to applied voltage suggests that the printed LM-based paste can function as a customizable electrothermal system, adaptable to seasonal environmental conditions in the target application area.

Fig. 6(a) shows the integrated de-/anti-icing system, in which a photothermal layer was coated on top of an electrothermal pattern. The Line 7 pattern was first printed using the electrothermal paste (ϕ_{Si} = 0.3) on the surface of the cured ARE matrix. The photothermal paste ($\phi_{PCM@Ga}$ = 0.3) was then applied at a thickness of 5 mm—matching that used in the mechanical loading tests—and cured in place. Notably, the catalyst-containing photothermal paste can solidify within days even without external heating (Fig. S8), offering a practical advantage for real-world outdoor applications. In practical scenarios, if accelerated curing is required, the paste can be applied to the target area and cured by indirect heating using hot-air blowers or space heaters, or, when necessary, by localized heat treatment. Such heating-assisted curing approaches are commonly adopted in coating and painting processes, and are therefore not expected to pose significant challenges for real-world implementation. For the laboratory-scale integrated system demonstrated below, the paste was cured at 150 °C for 2 hours, following the protocol established in our earlier study.[34] We note that the outermost photothermal layer, fabricated at the millimeter scale, behaves almost as a self-supporting bulk

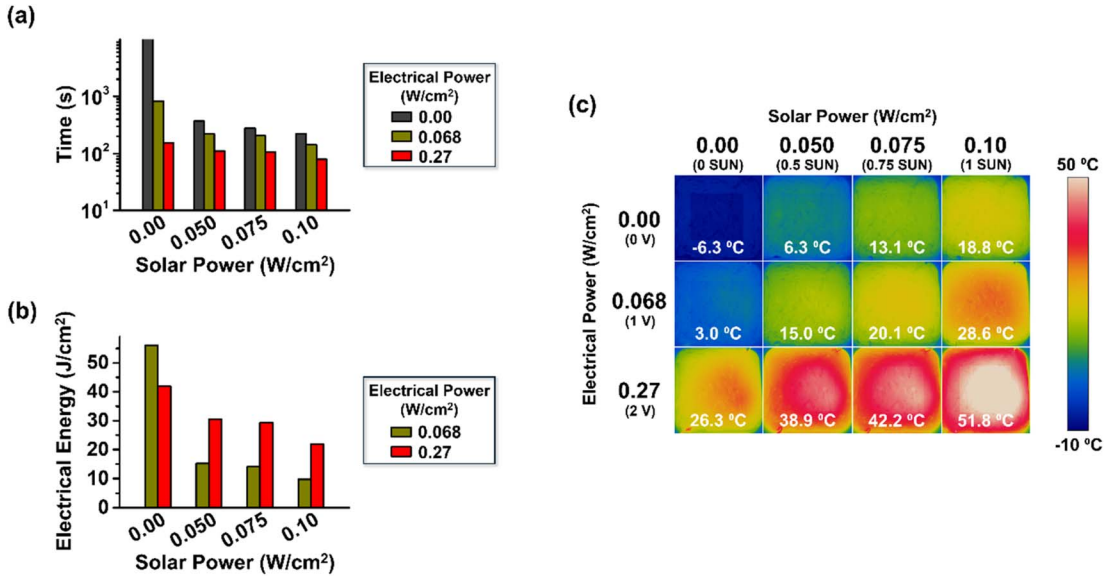

Fig. 7 (a) Time required for the system to reach the ice melting point (0 °C) under varying combinations of solar irradiation levels (0, 0.5, 0.75, and 1 sun) and electrical inputs (0, 1, and 2 V). (b) Energy consumption required to reach 0 °C at different simulated solar irradiation levels (0, 0.5, 0.75, and 1 sun) during electrothermal heating at different voltages (1 and 2 V). (c) IR images of the surface under different operation conditions, captured after 30 min.

material, thereby eliminating concerns about delamination that often arise in conventional micrometer-thick, film-type photothermal coatings. Although the cross-cut test (ASTM D3359)—typically used to evaluate the robustness of film/interface adhesion—is not strictly applicable to this bulk-type system, the result shown in Fig. S9 nonetheless demonstrates the strong structural integrity of the cured photothermal layer.

Fig. 6(b) and (c) illustrate the heating performance of the integrated de-/anti-icing system under subzero conditions (−20 °C), representative of winter environments, along with control data from the LM-free ARE matrix (see also SI Movie S1). In the control specimen, it took approximately 11 min under simulated sunlight (1 sun) for the surface temperature to exceed the melting point of ice (0 °C), with the peak temperature reaching only 9.7 °C after 90 min. In contrast, the LM-embedded integrated system exhibited a significantly faster temperature increase, surpassing 0 °C within 4 min and reaching 25.9 °C after 90 min under the same conditions. When operated solely in electrothermal mode (2 V, no sunlight), the surface temperature increased to 35.7 °C, outperforming the photothermal mode. These results demonstrate that the integrated system enables effective de-/anti-icing even in the absence of sunlight, such as under overcast or nighttime conditions. When both modes were simultaneously activated (1 sun and 2 V), the surface temperature exceeded 0 °C within only 1 min and reached the peak temperatures of the individual modes (25.9 °C and 35.7 °C) in just 9.7 and 16.6 min, respectively. Ultimately, a maximum surface temperature of 67.1 °C was achieved after 90 min, demonstrating the superior heating capacity of the dual-mode operation. The stability of this performance was further verified through 10 repeated dual-mode operation cycles without noticeable degradation, as shown in Fig. 6(d). The time required to reach the ice melting point (0 °C) and the maximum surface temperature was similar across repeated heating cycles, with average values of 60.8 ± 11.4 s and 66.3 ± 1.7 °C, respectively. In addition, the integrated system retained the same performance after more than six months of exposure to ambient conditions without special storage (Fig. S10–S12), confirming the absence of performance changes attributable to long-term sample degradation such as particle settling or phase separation.

Fig. 7(a) compares the time required for the integrated system to reach the ice melting point (0 °C) in a broader range of combined solar irradiation and electrical input power densities. The complete temperature evolution profiles for each condition are provided as raw data in Fig. S13. Even without any electrical input, the system was able to reach 0 °C within 278 s and 374 s under 0.075 W cm^{-2} (corresponding to 0.75 sun) and 0.05 W cm^{-2} (0.5 sun) conditions, respectively. These results demonstrate that the system can effectively perform de-/anti-icing using only solar energy, even on moderately overcast days. After 30 min of irradiation at this relatively low solar intensity, the surface temperatures reached 6.3 °C and 13.1 °C (Fig. 7(c)), respectively—well above the ice-melting point. These results are comparable to, and in some cases even slightly exceed, the performance of previously developed photothermal systems.[16]

In complete darkness (0 sun), simulating nighttime conditions, the application of electrical power became essential to increase the surface temperature. In many previously reported electrothermal de-/anti-icing systems, the typical applied power ranges from 0.1 to 1 W cm^{-2}.[42] Remarkably, applying only 0.068 W cm^{-2} (1 V) enabled the system to reach the ice melting point within 820 s, even without solar irradiation. Furthermore, the combination of solar irradiation with electrical input exhibited a clear synergistic effect: as the solar intensity increased, the time required to reach 0 °C progressively decreased under the

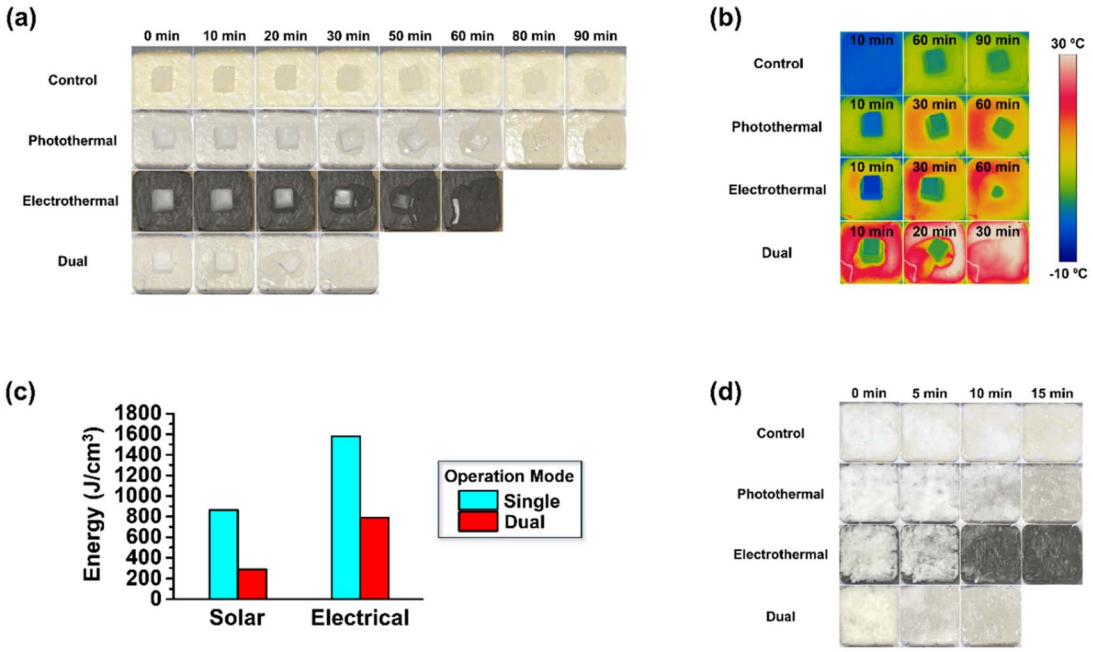

Fig. 8 (a) Evaluation of the de-icing performance using ice cubes (2.5 cm × 2.5 cm × 2.5 cm) in different operation modes. (b) IR images of melting ice cubes on the surface, taken at selected time intervals. (c) The solar and electrical energy consumed to completely melt the ice block in single- and dual-operation mode. (d) De-icing performance test under full-surface ice coverage. All experiments were conducted in a subzero environment (−20 °C). The 'control' refers to tests conducted using the LM-free ARE matrix.

same voltage condition. Under full sunlight (1 sun, 0.1 W cm^{-2}), applying 0.068 W cm^{-2} (1 V) and 0.27 W cm^{-2} (2 V) resulted in a time-to-0 °C difference of only ≈1 min. However, the integrated electrical energy consumption at 0.068 W cm^{-2} (9.72 J cm^{-2}) was only ≈44.4% that at 0.27 W cm^{-2} (21.89 J cm^{-2}) (Fig. 7(b)). This indicates that the use of minimal electrical power, when combined with solar input, can achieve nearly equivalent de-/anti-icing performance with significantly improved energy efficiency. These findings highlight the system's adaptability and energy-saving potential under variable environmental conditions. In practical applications, the electrothermal pattern beneath the photothermal layer can be readily reconfigured—thanks to the printable nature of the LM-based paste—to optimize the trade-off between heating performance and power consumption. This design flexibility offers a distinct advantage over conventional de-/anti-icing systems equipped with electrothermal functions, where electrical properties are often fixed by material composition.

Fig. 8(a)–(d) and S14 demonstrate the practical de-/anti-icing capabilities of the integrated system in different operation modes (see also SI Movies S2 and S3). As expected, a water droplet placed on the surface of the integrated system remained unfrozen for an extended duration under electrothermal or dual-mode operation (Fig. S14), both of which achieve higher surface temperatures than the photothermal mode—where freezing was already absent (Fig. 3(i)). This confirms the system's ability to effectively prevent the freezing of liquid water in subzero environments. However, to be practically viable in real-world scenarios, the system must not only prevent the formation of ice but also efficiently melt rigid, preformed ice, which is mechanically and thermally more demanding. To assess this, a solid ice cube (2.5 cm × 2.5 cm × 2.5 cm) was placed on the surface of the system in a cold environment (−20 °C), followed by activation by light and/or electrical stimuli (Fig. 8(a)). When tested on the LM-free ARE matrix under simulated sunlight (1 sun), the ice cube remained partially unmelted even after 90 min, highlighting the limited thermal capacity of the control specimen. IR imaging revealed that the temperature of the ice cube itself was significantly lower than that of the underlying heated surface (Fig. 8(b)), indicating that a substantial thermal gradient—achievable only through elevated surface temperatures—is required to melt thick ice structures. This highlights a critical design consideration for ice management systems targeting the removal of heavy or accumulated ice. In sharp contrast, the same-sized ice block was completely melted on the LM-embedded, integrated system surface in both photothermal and electrothermal modes, taking 90 min and 70 min, respectively. These melting times correlate well with the temperature evolution profiles shown in Fig. 6(b) and (c). Notably, when operated in dual-mode, the ice cube was fully melted in just 30 minutes—corresponding to only 33.3% and 42.9% of the durations required by photothermal and electrothermal modes alone, respectively. We calculated the total energy consumed to completely melt the ice block in each operation mode (Fig. 8(c)). Under 1 sun solar irradiation (0.1 W cm^{-2}) for 90 min, the energy consumed per unit ice-block volume was 864 J cm^{-3}, whereas during dual-mode operation for 30 min, the corresponding solar energy input decreased significantly to 288 J cm^{-3}. Similarly, at an applied voltage of 2 V (0.27 W cm^{-2}) for 60 min in the electrothermal mode, the electrical energy consumed per unit ice-block volume was 1578.1 J cm^{-3}, while during dual-mode operation for 30 min,

the required electrical energy was reduced by nearly half to 789.0 J cm^{-3}. These results clearly demonstrate the enhanced ice-melting efficiency afforded by dual-mode operation. (Note: due caution should be exercised when comparing these energy consumption with those reported in other studies, as the dynamics of ice melting can depend on the specific ice formation conditions.)

A more practically challenging condition was also tested, in which the surface was entirely covered by an opaque ice layer (Fig. 8(d)), preventing incident sunlight from directly reaching the photothermal layer. Under this scenario, both the LM-free matrix and the integrated system showed similarly poor de-icing performance in the first 10 min of photothermal-only operation. However, as the surface ice began to melt and reveal portions of the photothermal surface, the LM-based system gradually outperformed the control. Conversely, the electrothermal mode was not affected by the initial ice coverage, as heating originated from beneath the ice. In this case, partial melting occurred after 10 min, and complete melting was achieved within 15 min. Notably, even though photothermal heating was initially inactive when used alone, it contributed significantly when operated in dual mode. Electrothermal heating rapidly created exposure sites for light to reach the photothermal surface, initiating its activation. Consequently, complete melting of the ice layer was achieved within just 10 min—representing the fastest de-icing observed across all tested modes. These results emphasize the practical utility of dual-mode operation for overcoming real-world de-icing challenges, including those posed by surface-wide opaque ice layers.

Conclusion

In this study, an integrated photo/electrothermal dual-mode de-/anti-icing system was developed using Ga-based LMs. In comparison with previously reported dual-mode photo/electrothermal de-/anti-icing systems, the present platform distinguishes itself in its structural form factor and integration strategy while providing comparable heating performances. Unlike conventional systems fabricated as thin films, which may require pre-fabrication, substrate transfer, and complex lamination steps, our approach utilizes two viscoelastic, paste-type modules that can be directly applied onto arbitrary substrates. This liquid-state, conformable configuration allows *in situ* coating and patterning, providing superior processability and scalability compared with film-based architectures. Moreover, the photothermal and electrothermal components are independently formulated and tunable, enabling mode-specific optimization according to environmental or operational conditions—a feature unattainable in monolithic film designs. Although bulk Ga is not a low-cost material, the process simplicity demonstrated here can significantly lower the overall fabrication cost. Moreover, unlike traditional LMs such as Hg or Pb, Ga is non-volatile[20] and biocompatible,[28–30] and exhibits low environmental reactivity under normal conditions,[43] while also being recyclable,[36] making it a promising and sustainable material choice for de-/anti-icing systems.

While bulk Ga is a poor photothermal converter under broadband solar irradiation, its photothermal efficiency significantly improves when micronized and encapsulated within a composite matrix, enabling effective de-/anti-icing using only sunlight during daytime, without external power input. To prevent an excessive temperature increase during warmer seasons, a PCM with a melting temperature of ≈37 °C was hybridized with Ga, forming a self-thermally regulating photothermal agent (PCM@Ga) capable of absorbing latent heat during phase transitions. The photothermal heating layer, formulated by dispersing PCM@Ga into an ARE matrix, exhibited seasonally adaptive solar-to-thermal conversion performance, achieving $\Delta T \approx 40$ °C and $\Delta T \approx 15$ °C under 1 sun irradiation at −20 °C and 25 °C, respectively. Increasing the hybrid filler content in the uncured ARE matrix enhanced the rheological processability while maintaining heating performance under cold conditions. Upon curing, composites with optimized filler ratios ($\phi_{PCM@Ga} = 0.2$ and 0.3) exhibited superior mechanical strength, withstanding compressive loads up to 100 kN. In parallel, a printable electrothermal system was developed using bulk-phase EGaIn as the conductive matrix. Its rheological properties were easily tuned by incorporating Si particles compatible with LM, yielding a viscoelastic colloidal suspension suitable for patternable printing. By varying the printed pattern geometry or the applied voltage, a broad and tunable heating range was achieved, ensuring reliable operation even during overcast weather or nighttime—conditions where photothermal systems alone would be insufficient. Both photothermal and electrothermal components with paste-type formulations can be easily integrated on various target surfaces *via* sequential application, thereby forming an integrated system capable of effective de-/anti-icing under simulated winter conditions, including overcast and nighttime scenarios, using light and/or electrical power. This approach offers practical utility for cold-environment safety management in roads, aircraft, outdoor equipment, buildings, and other infrastructure applications.

Conflicts of interest

There are no conflicts of interest to declare.

Data availability

The data supporting this article have been included as part of the supporting information (SI). Supplementary information: experimental details; size distributions of the PCM and PCM@Ga microdroplets; SEM-EDS analysis of a fully encapsulated PCM@Ga particle; photograph of the mixing unit after mixing uncured photothermal pastes with different PCM@Ga loadings; photograph of micronized Ga powder and the corresponding SEM image, together with its size distribution; photographs of the disk-shaped ARE composites with and without LM; surface temperature profile of the cured LM-free ARE matrix under simulated solar irradiation at ambient temperature; DSC profiles of the cured composite for the as-prepared sample and after six months of storage under

ambient conditions; visual appearance of the cured LM-free ARE matrix after a compression test; electrical resistances of sing-line patterns fabricated using electrothermal pastes with different Si loadings; DSC profiles of the uncured ARE matrix and the naturally cured photothermal paste at room temperature; photograph of the cured photothermal composite after performing the cross-cut adhesion test; repeatability of dual-mode heating performance of the integrated system after six months of ambient storage; average surface temperature profiles of the integrated system under varying solar irradiation levels and electrical inputs; evaluation of the anti-icing performance of the integrated system using water droplets; calculation method for photothermal conversion efficiency. SI Movies: surface heating behavior of the LM-embedded integrated photo/electrothermal system in various operation modes (720× speed); evaluation of de-icing performance using ice cubes in different operation modes (580× speed); de-icing performance test under full-surface ice coverage (180× speed). See DOI: https://doi.org/10.1039/d5ta10376b.

Acknowledgements

This work was supported by the National Research Foundation of Korea (NRF) grant funded by the Korea government (MSIT) (RS-2025-16065277 and RS-2023-00259995). This research was also supported by the Basic Science Research Program through the National Research Foundation of Korea (NRF) funded by the Ministry of Education (RS-2025-25421959, RS-2024-00460455). We also greatly appreciate Dr Jong-Wook Han at the Hybrid Structural Testing Center (HySTeC) for his kind support in performing mechanical property evaluation using 100 kN UTM.

References

1 S. B. Hong and H. S. Yun, Predicting Black Ice-Related Accidents with Probabilistic Modeling Using GIS-Based Monte Carlo Simulation, *PLoS One*, 2024, **19**, e0303605.
2 Y. Cao, W. Tan and Z. Wu, Aircraft Icing: An Ongoing Threat to Aviation Safety, *Aerosol. Sci. Technol.*, 2018, **75**, 353–385.
3 W. Wang, W. Peng, L. Tong, X. Tan and T. Xin, Study on Sustainable Development of Power Transmission System Under Ice Disaster Based on a New Security Early Waning Model, *J. Clean. Prod.*, 2019, **228**, 175–184.
4 A. J. Meuler, G. H. McKinley and R. E. Cohen, Exploiting Topographical Texture to Impart Icephobicity, *ACS Nano*, 2010, **4**, 7048–7052.
5 J. Lv, Y. Song and J. Wang, Bio-Inspired Strategies for Anti-Icing, *ACS Nano*, 2014, **8**, 3152–3169.
6 R. Chatterjee, D. Beysens and S. Anand, Delaying Ice and Frost Formation Using Phase-Switching Liquids, *Adv. Mater.*, 2019, **31**, 1807812.
7 E. Mitridis, T. M. Schutzius, A. Sicher, C. U. Hail, H. Eghlidi and D. Poulikakos, Metasurfaces Leveraging Solar Energy for Icephobicity, *ACS Nano*, 2018, **12**, 7009–7017.
8 Y. Liu, Y. Wu, Y. Liu, R. Xu, S. Liu and F. Zhou, Robust Photothermal Coating Strategy for Efficient Ice Removal, *ACS Appl. Mater. Interfaces*, 2020, **12**, 46981–46990.
9 S. Wu, Y. Du, Y. Alsaid, D. Wu, M. Hua, Y. Yan, B. Yao, Y. Ma, X. Zhu and X. He, Superhydrophobic Photothermal Icephobic Surfaces Based on Candle Soot, *Proc. Natl. Acad. Sci. U. S. A.*, 2020, **117**, 11240–11246.
10 H. Zhang, G. Zhao, S. Wu, Y. Alsaid, W. Zhao, X. Yan, L. Liu, G. Zou, J. Lv, X. He, Z. He and J. Wang, Solar Anti-Icing Surface with Enhanced Condensate Self-Removing at Extreme Environmental Conditions, *Proc. Natl. Acad. Sci. U. S. A.*, 2021, **118**, e2100978118.
11 P. Wang, T. Yao, Z. Li, W. Wei, Q. Xie, W. Duan and H. Han, A Superhydrophobic/Electrothermal Synergistically Anti-Icing Strategy Based on Graphene Composite, *Compos. Sci. Technol.*, 2020, **198**, 108307.
12 X.-M. Xie, J.-F. Su, Y.-D. Guo and L.-Q. Wang, Evaluation of A Cleaner De-Icing Production of Bituminous Material Blending with Graphene by Electrothermal Energy Conversion, *J. Clean. Prod.*, 2020, **274**, 122947.
13 X. Su, H. Li, X. Lai, Z. Yang, Z. Chen, W. Wu and X. Zeng, Vacuum-Assisted Layer-by-Layer Superhydrophobic Carbon Nano tube Films with Electrothermal and Photothermal Effects for Deicing and Controllable Manipulation, *J. Mater. Chem. A*, 2018, **6**, 16910–16919.
14 T. Hao, Z. Zhu, H. Yang, Z. He and J. Wang, All-Day Anti-Icing/Deicing Film Based on Combined Photo-Electro-Thermal Conversion, *ACS Appl. Mater. Interfaces*, 2021, **13**, 44948–44955.
15 S. Peng, X. Xiao, J. Wei and J. Wang, Superhydrophobic Coating with Electro-Photo-Thermal Conversion Properties for All-Weather Anti-Icing, *Sol. Energy*, 2024, **270**, 112384.
16 Z. Zhao, Y. Wang, Z. Wang, X. Cui, G. Liu, Y. Zhang, Y. Zhu, J. Chen, S. Sun, K. Zhang, X. Liu and H. Chen, A New Composite Material with Energy Storage, Electro/Photo-Thermal and Robust Super-Hydrophobic Properties for High-Efficiency Anti-Icing/De-Icing, *Small*, 2024, **20**, 2311435.
17 J.-J. Liu, C.-Y. He, B.-H. Liu, Z.-Q. Wang, S.-J. Zhao, Z.-W. Lu, Y.-Z. Zhang, Z.-Q. Tang, X.-H. Gao and X. Aday, A Robust Photo-Thermal and Electro-Thermal Superhydrophobic Surface for All-Weather Anti-Icing/Deicing, *Chem. Eng. J.*, 2024, **489**, 151338.
18 W. Feng, Z. Xie, H. Wang, R. Chen, X. Zhu, Y. Ding and Q. Liao, All-Weather Anti-Icing and De-Icing Properties of the Carbon-Based Electro@Photo-Thermal Material with Adaptive Temperature Control Performance, *Prog. Org. Coat.*, 2024, **188**, 108194.
19 X. Cui, Q. Ruan, X. Zhuo, X. Xia, J. Hu, R. Fu, Y. Li, J. Wang and H. Xu, Photothermal Nanomaterials: A Powerful Light-to-Heat Converter, *Chem. Rev.*, 2023, **123**, 6891–6952.
20 T. Daeneke, K. Khoshmanesh, N. Mahmood, I. A. de Castro, D. Esrafilzadeh, S. J. Barrow, M. D. Dickey and K. Kalantar-Zadeh, Liquid Metals: Fundamentals and Applications in Chemistry, *Chem. Soc. Rev.*, 2018, **47**, 4073–4111.

21 S.-Y. Tang, C. Tabor, K. Kalantar-Zadeh and M. D. Dickey, Gallium Liquid Metal: The Devil's Elixir, *Annu. Rev. Mater. Res.*, 2021, **51**, 381–408.
22 M. Zare and K. S. Mikkonen, Phase Change Materials for Life Science Applications, *Adv. Funct. Mater.*, 2023, **33**, 2213455.
23 S. Kang, W. Kim, C. Song, Y. Hong, S. Kim, M. Goh, S. K. Chung and J. Lee, Novel Latent Heat Storage Systems Based on Liquid Metal Matrices with Suspended Phase Change Material Microparticles, *ACS Appl. Mater. Interfaces*, 2023, **15**, 36781–36791.
24 H. Lee, J. Park, M. Kang, W. Kim, S. K. Chung and J. Lee, Macroscopic Phase-Change Drug Carrier Ball with Photothermally Controlled Release and Magnetically Controlled Transport Properties, *Adv. Mater. Technol.*, 2025, **10**, e00694.
25 S. Kim, S. Kang and J. Lee, High-Thermal-Conductivity and High-Fluidity Heat Transfer Emulsion with 89 wt% Suspended Liquid Metal Microdroplets, *ACS Omega*, 2023, **8**, 17748–17757.
26 Z. Wei, C. Cai, Y. Huang, Y. Wang and Y. Fu, Biomimetic Surface Strategy of Spectrum-Tailored Liquid Metal via Blackbody Inspiration for Highly Efficient Solar Steam Generation, Desalination, and Electricity Generation, *Nano Energy*, 2021, **86**, 106138.
27 S. Jamalzadegan, M. Zare, M. J. Dickens, F. Schenk, A. Velayati, M. Yarema, M. D. Dickey and Q. Wei, Shape and Size-Dependent Surface Plasmonic Resonance of Liquid Metal Alloy (EGaIn) Nanoparticles, *Nanoscale*, 2015, **17**, 22819–22833.
28 X. Zhu, M. Duan, L. Zhang, J. Zhao, S. Yang, R. Shen, S. Chen, L. Fan and J. Liu, Liquid Metal-Enabled Microspheres with High Drug Loading and Multimodal Imaging for Artery Embolization, *Adv. Funct. Mater.*, 2023, **33**, 2209413.
29 P. Zhu, S. Gao, H. Lin, X. Lu, B. Yang, L. Zhang, Y. Chen and J. Shi, Inorganic Nanoshell-Stabilized Liquid Metal for Targeted Photonanomedicine in NIR-II Biowindow, *Nano Lett.*, 2019, **19**, 2128–2137.
30 N. Xia, N. Li, W. Rao, J. Yu, Q. Wu, L. Tan, H. Li, L. Gou, P. Liang, L. Li and X. Meng, Multifunctional and Flexible ZrO_2-Coated EGaIn Nanoparticles for Photothermal Therapy, *Nanoscale*, 2019, **11**, 10183–10189.
31 S. Yang, H. Zhang, X. Sun, J. Bai and J. Zhang, 3D-Printed Liquid Metal-in-Hydrogel Solar Evaporator: Merging Spectrum-Manipulated Micro-Nano Architecture and Surface Engineering for Solar Desalination, *ACS Nano*, 2024, **18**, 5847–5863.
32 X. Huang, J. Liu, P. Zhou, G. Su, T. Zhou, X. Zhang and C. Zhang, Ultrarobust Photothermal Materials via Dynamic Crosslinking for Solar Harvesting, *Small*, 2022, **18**, 2104048.
33 S. Yang, Y. He, J. Bai and J. Zhang, Synergistic Dual-Mechanism Localized Heat Channeling and Spectrum-Taiolored Liquid Metal Hydrogels for Efficient Solar Water Evaporation and Desalination, *Small*, 2023, **19**, 2302526.
34 S. Kim, C. Song, S. Kim, S. Kang, H. G. Menge, Y. T. Park and J. Lee, Effects of a Liquid Metal Co-filler on the Properties of Epoxy/Binary Filler Composites, *J. Appl. Polym. Sci.*, 2024, **141**, e55134.
35 Y. Shen, D. Boylan, F. Chen, F. Guo, M. He and X. Dai, High-Efficiency Frost and Ice Control via Sensing-Assisted Nonvibrational Slippery Surfaces, *J. Mater. Chem. A*, 2025, **13**, 16797–16806.
36 H. Chang, P. Zhang, Y. Cui, Y. Hou, Z. Sun and W. Rao, Recoverable Liquid Metal Paste with Reversible Rheological Characteristic for Electronics Printing, *ACS Appl. Mater. Interfaces*, 2020, **12**, 14125–14135.
37 K. Doudrick, S. Liu, E. M. Mutunga, K. Klein, V. Damle, K. K. Varanasi and K. Rykaczewski, Different Shades of Oxide: From Nanoscale Wetting Mechanisms to Contact Printing of Gallium-Based Liquid Metals, *Langmuir*, 2014, **30**, 6867–6877.
38 Y. Wu, X. Huang, L. Huang, X. Guo, R. Ren, D. Liu, D. Qu and J. Chen, Self-Healing Liquid Metal and Si Composite as High-Performance Anode for Lithium-Ion Batteries, *ACS Appl. Energy Mater.*, 2018, **1**, 1395–1399.
39 B. Han, Y. Yang, X. Shi, G. Zhang, L. Gong, D. Wu, H. Zeng, C. Wang, M. Gu and Y. Deng, Spontaneous Repairing Liquid Metal/Si Nanocomposite as a Smart Conductive-Additive-Free Anode for Lithium-Ion Battery, *Nano Energy*, 2018, **50**, 359–366.
40 B.-W. Zhang, L. Ren, Y.-X. Wang, X. Xu, Y. Du and S.-X. Dou, Gallium-Based Liquid Metals for Lithium-Ion Batteries, *Interdiscip. Mater.*, 2022, **1**, 354–372.
41 W. Jung, M. H. Vong, K. Kwon, J. U. Kim, S. J. Kwon, T. Kim and M. D. Dickey, Giant Decrease in Interfacial Energy of Liquid Metals by Native Oxides, *Adv. Mater.*, 2024, **36**, 2406783.
42 H. Gao, Y. Zhou, J. Ma, H. Jin, J. Bao and D. Wen, Recent Advancements in Electro-Thermal Anti-/De-icing Materials, *RSC Adv.*, 2025, **15**, 17102–17115.
43 S. Chen, R. Zhao, X. Sum, H. Wang, L. Li and J. Liu, Toxicity and Biocompatibility of Liquid Metals, *Adv. Healthcare Mater.*, 2022, **12**, 2201924.